RSC Advances

PAPER

View Article Online
View Journal | View Issue

Cite this: *RSC Adv.*, 2022, **12**, 34080

Enhancement of photocatalytic efficacy by exploiting copper doping in nano-hydroxyapatite for degradation of Congo red dye†

Md. Sahadat Hossain,[a] Supanna Malek Tuntun,[ab] Newaz Mohammed Bahadur[b] and Samina Ahmed *[ac]

This research deals with the photocatalytic activity of hydroxyapatite and the improvement of efficiency by doping various percentages of copper; the catalysts were synthesized by the wet-chemical method. Pure and copper-doped photocatalysts were characterized by several techniques including X-ray diffraction (XRD), Fourier Transform Infrared (FTIR) spectroscopy, Raman spectroscopy, scanning electron microscopy (SEM), thermogravimetric analysis (TGA), dynamic scanning calorimetry (DSC), and UV-Vis spectroscopy. The competency of pure and copper-doped hydroxyapatite as photocatalysts was assessed by their interaction with Congo red dye. The crystallographic parameters of the catalysts were also estimated by employing the XRD technique, and a relationship was established between the calculated parameters and photocatalytic performance. Crystallite size was calculated from various model equations, which revealed an acceptable crystallite size of 42–68 nm. Copper doping in hydroxyapatite impressively augmented the photocatalytic efficacy, for example 99% dye was degraded upon 0.63% Cu-doping compared to 75% for the pure HAp, which was exemplified not only by the reaction rate but also by the quantum yield. The degradation percentages changed with time but became fixed at 200 min. The molar extinction coefficient was estimated by employing the Beer–Lambert law and further utilized to compute the photonic efficiency of the catalysts. In the study of the photochemical reaction, a simplified reaction process was proposed, and the potentials of the conduction band and valence band were assessed, which influenced the activity. The doping of Cu in crystalline hydroxyapatite will enhance the photocatalytic activity towards Congo red dye under all experimental conditions.

Received 6th October 2022
Accepted 15th November 2022

DOI: 10.1039/d2ra06294a

rsc.li/rsc-advances

1. Introduction

The versatile application of hydroxyapatite (HAp) has made this material special to researchers in diverse fields, such as biochemists, chemists, environmental engineers, materials scientists, doctors, dentists, and so on. One of the main fields of application of HAp is photocatalysis. A few important applications of HAp as a catalyst are the degradation of methylene blue (MB) and doxycycline drug,[1] and volatile organic compounds,[2] the deoxygenation of bio-oil,[3] the conversion of lignin derivatives into small molecular acids,[4] the degradation of bisphenol A,[5] the formation of carbon–nitrogen bonds,[6] the synthesis of alkenes,[7] the oxidation of silanes,[8] *etc.* HAp singly or in combination with other materials is widely utilized to degrade organic pollutants. It is one of the most widely used biomaterials for the treatment of wastewater in addition to its application as a biomaterial. It is a promising calcium phosphate-based adsorbent possessing versatility and an inspiring adsorptive property.[9] This sorption property generates secondary pollutants that also create another issue for a clean environment. Fenton and photo-Fenton processes are other widely used methods for wastewater treatment that also have a few inherent shortcomings such as a narrow pH range of application, non-recyclability of iron, *etc.*[10] To eliminate the secondary pollutants, broad application range photodegradation is the best choice for dye[11] and antibiotics[12] remediation using HAp. HAp alone cannot achieve photodegradation with high catalytic efficiency of contaminants in the presence of a light source. Thus, HAp is incorporated with some other strong photocatalysts such as TiO, ZnO, Zn, CdS, Ag, Ag/Fe, Co, Ni, *etc.* in a composite or doped form.[12–17] Copper is another doping element for the HAp crystal and has recently been used in Fenton-like Cu doped HAp either alone or in combination

[a]*Glass Research Division, Institute of Glass & Ceramic Research and Testing, Bangladesh Council of Scientific and Industrial Research (BCSIR), Dhaka 1205, Bangladesh*

[b]*Department of Applied Chemistry and Chemical Engineering, Noakhali Science and Technology University, Noakhali, Bangladesh*

[c]*BCSIR Laboratories Dhaka, Bangladesh Council of Scientific and Industrial Research (BCSIR), Dhaka 1205, Bangladesh. E-mail: shanta_samina@yahoo.com*

† Electronic supplementary information (ESI) available. See DOI: https://doi.org/10.1039/d2ra06294a

with other elements,[10,18] in polycaprolactone encapsulated HAp,[19] to enhance biocompatibility,[20] *etc.*

Water pollution, which is increasing day by day, has been creating problems causing numerous adverse effects on the aquatic environment. Only 0.6% of the total amount of water in the universe is available for drinking and other use by humans.[21] The worldwide imbalance in aquatic environs has originated mainly from textile effluent (mostly dyes),[22] active pharmaceutical ingredients (APIs),[23] industrial chemicals and pesticides,[24] the tanning industry, the electroplating industry, metal smelting, batteries, petrochemicals, paper manufacturing and electrolysis,[25] biocides, polycyclic aromatic hydrocarbons (PAHs), illicit drugs, herbicides, surfactants,[26] *etc.*

Dyestuffs are not only used in the textile industries to color cloths but also in other chemical industries such as in pharmaceuticals to color medicine, in food manufacturing to impart color appeal, in beverages to make color solutions, *etc.* Nearly 10 000 various commercial dyes are available on the world market with an approximate production of 0.70 million tons, of which 10–25% is discharged as unbound effluent.[27] Polluted water due to textile effluent is responsible for ecotoxicological dangers with adverse effects on living organisms resulting in serious problems in human health such as dermatitis, skin irritation, allergies, and mutations.[28] Dyestuffs also impede the penetration of sunlight, which is compulsory for photosynthesis in the aquatic environment, thus hampering the natural growth of flora and fauna.[29]

A number of processes/techniques are applied to get rid of hazardous textile effluent (dyes) such as electro-peroxone,[30] precipitation, membrane filtration, flotation, adsorption, coagulation, electro-coagulation, ion exchange,[31] photocatalysis, irradiation,[32] haloalkaliphilic bacterial consortium,[33] electro-coagulation and electro-Fenton,[34] Fenton and photo-Fenton processes,[35] biocatalytic treatment,[36] *etc.* All the processes described here have inherent advantages and disadvantages and are chosen based on feasibility study. In addition to the dyes, pharmaceutical active ingredients, especially various kinds of antibiotics, are also causing problems in uncontaminated water owing to their harmfulness and long-term persistence.[37] The presence of antibiotics in the aquatic environment causes bacteria and virus resistance to antibiotics. According to the CDC 2019 report, nearly 2.8 million antibiotic-resistant infections happen in the U.S. every year with the death of more than 35 000 people.[38]

In this research, copper metal was taken into consideration as a doping material in HAp to prepare an excellent photocatalytic substance that was assessed in the degradation of Congo red dye. A crystallographic relationship was also found between the crystal structure/crystallographic parameters and photocatalytic activity of pure and copper-doped HAp. A number of characterization methods were performed to obtain an in-depth understanding of the pure and Cu-doped HAp. The efficiency of the catalyst under a halogen lamp was also compared with that under sunlight. Another target of this research was to find out the photodegradation kinetics along with the quantum yield.

2. Materials and methods

2.1. Materials

Calcium hydroxide [$Ca(OH)_2$], orthophosphoric acid [H_3PO_4], cupric oxide [CuO], nitric acid [HNO_3], and ammonium hydroxide [NH_4OH] were purchased from E-Merck Germany. Congo red was bought from Shanghai Chemical Reagent, China. Deionized water (DI) was prepared after a double distillation process in the Glass Research Division laboratory.

2.2. Preparation of pure and Cu-doped hydroxyapatite

A conventional wet chemical precipitation technique was employed to synthesize HAp from calcium hydroxide [$Ca(OH)_2$] of 99% purity and *ortho*-phosphoric acid [H_3PO_4] as an 85% (w/w) solution maintaining a Ca/P ratio of 1.67.[39] Various percentages (0.32, 0.63, 1.25, 2.5, and 5) of Cu-doped hydroxyapatite (Cu-HAp) were prepared following the same methodology and preserving copper and calcium total percentages of 100. For the synthesis of HAp, equal volumes (100 mL) of a 1.67 M colloidal solution of $Ca(OH)_2$ and 1.0 M solution of H_3PO_4 solution were prepared with the aid of DI water, and the latter was slowly (3 mL min^{-1}) added to the former at fixed reaction parameters (pH = 10–11, temp = 25 °C, continuous stirring). Next, the formed precipitate was filtered after 6 h and oven-dried at 105 °C for 24 h. After that, the dried sample was powdered using a hand mortar and subjected to calcination at 900 °C (increment rate = 3.5 °C min^{-1}) for 30 min. In the case of Cu-HAp synthesis, 100 mL of a 1.67 M CuO solution was prepared using HNO_3 and a fixed volume (0.32, 0.63, 1.25, 2.5, and 5 mL) was added to H_3PO_4 while removing the same volume of $Ca(OH)_2$, and subsequent steps were the same as the previously mentioned procedure. Eqn (1)–(3) describe the chemical reactions associated with the synthesis of HAp as well as Cu-HAp, and the process is illustrated in Scheme S_1 as a ESI file.†

$$CuO + 2HNO_3 \rightarrow \text{Cu-solution} \quad (1)$$

$$10Ca(OH)_2 + 6H_3PO_4 \rightarrow Ca_{10}(PO_4)_6(OH)_2 \quad (2)$$

$$xCa(OH)_2 + y\text{Cu-solution} + 6H_3PO_4 \rightarrow Ca_{x-y}Cu_y(PO_4)_6(OH)_2 \quad (3)$$

2.3. Characterization

Crystallographic information was collected using a Rigaku SE X-ray diffraction (XRD) machine equipped with a Cu radiation source, 20 °C operating temperature, scanning range of 2θ = 15–70°, steps of 0.01, and operating conditions of 40 mA and 50 kV. The data of the powder samples were collected using Bragg–Brentano geometry and compared with the standard ICDD database, and the machine was calibrated using a standard silicon reference. Crystallographic parameters such as lattice parameters, crystallinity, dislocation density, microstrain, crystallinity index, HAp percentage, β-tricalcium phosphate (β-TCP) percentage, and volume fraction of β-TCP were calculated

by employing eqn (4)–(11) and the details of these equations are discussed elsewhere.[39]

$$\text{Lattice parameter equation}: \left(\frac{1}{d_{hkl}}\right)^2 = \frac{4}{3}\left(\frac{h^2+hk+k^2}{a^2}\right) + \frac{l^2}{c^2} \quad (4)$$

$$\text{Crystallite size}: D_c = \frac{K\lambda}{\beta \cos\theta} \quad (5)$$

$$\text{Dislocation density}: \delta = \frac{1}{(D_c)^2} \quad (6)$$

$$\text{Degree of crystallinity}: X_c = \left(\frac{K_a}{\beta}\right)^3 = \left(\frac{0.24}{\beta}\right)^3 \quad (7)$$

$$\text{Crystallinity index}: \text{CI}_{\text{XRD}} = \sum \frac{H_{(202)} + H_{(300)} + H_{(112)}}{H_{(211)}} \quad (8)$$

$$\text{Percentage of HAp} = \frac{I_{\text{HA}(211)}}{I_{\text{HA}(211)} + I_{\beta\text{-TCP}(0210)}} \quad (9)$$

$$\text{Percentage of } \beta\text{-TCP} = \frac{I_{\beta\text{-TCP}(0210)}}{I_{\text{HA}(211)} + I_{\beta\text{-TCP}(0210)}} \quad (10)$$

$$\text{Volume fraction of } \beta\text{-TCP}: X_B = \frac{PW_B}{1+(P-1)W_B} \quad (11)$$

where d_{hkl} = interplanar distance; a, b, c, h, k, and l = lattice parameters; D_c = crystallite size, K = shape factor (arbitrary constant)/Scherrer's constant = 0.94; λ = 1.5406 = wavelength of the copper source; β = FWHM (full width at half maximum) in radian, θ = diffraction angle (in degree), δ = dislocation density, X_c = degree of crystallinity, K_a = a constant = 0.24 for HAp, CI_{XRD} = crystallinity index, $H_{(hkl)}$ = peak height of the respective plane, $I_{\beta\text{-TCP/HA}(hkl)}$ = intensity of β-TCP/HA for the respective plane, P = 2.275 = integrated intensity of HAp; W_B = β-TCP percentage.

An FTIR spectrometer (IR-Prestige 21, Shimadzu, Japan) was applied to identify the functional groups, and the machine was operated using the attenuated total reflectance (ATR) mode. The data were collected using 30 scans and a spectral resolution of 4 cm^{-1} for the scanning range of 4000 to 400 cm^{-1}.

In addition to the FTIR analysis, Raman mapping was also performed to identify functional groups. A HORIBA Macro-RAM™ instrument was engaged to perform this identification using a 785 nm wavelength light source with a mapping range from 3400 cm^{-1} to 100 cm^{-1}. The surface morphology of the synthesized products was inspected with the assistance of a Phenom Pro scanning electron microscopy (SEM) machine with an accelerating voltage of 10 kV. Thermogravimetric analysis (TGA) and Differential scanning calorimetry (DSC) were performed using a simultaneous thermal analysis machine (NETZSCH STA 449F5 STA449F5B-0167-M) within the range of 30–1200 °C at a heating rate of 20 °C min^{-1} in a nitrogen atmosphere. The optical band gap was measured using the absorption frequency in a UV-Vis spectrophotometer, and the value was calculated using the Tauc method as presented in eqn (12) for direct band gaps.[11,40]

$$\alpha\hbar\theta = A(\hbar\theta - E_g)^n \quad (12)$$

where α = absorption co-efficient, $\hbar$ = Plank's constant, θ = frequency of a photon, A = a constant, E_g = band gap of the material, and n = 2 for a direct band gap or 1/2 for an indirect band gap.

2.4. Photocatalytic activity

The photocatalytic activity of the prepared samples was assessed by utilizing an in-house built halogen lamp (SEN TAI JM-500) of 500 W equipped with a cooling water circulating system. If not mentioned otherwise, the sample conditions were maintained at fixed values such as a concentration at 20 ppm, solution volume of 50 mL, operating temperature of 25 °C, pH at neutral, irradiation time of 180 min, sample to light distance of 14 cm, and humidity of 60%. UV-Vis spectrophotometry was employed to quantify the photodegradation. The percentage and capacity of photodegradation were estimated using eqn (13) and (14). The degradation percentage (Dp) of the samples was computed by utilizing the following eqn (13), where C_0 and C_t represent the initial and final (at time "t") concentrations, respectively.[27] The removal capacity (q_e) of the photocatalyst was calculated with the aid of eqn (14), where W and V denote the weight of the catalyst and the volume of the aqueous solution of the dye, respectively. The degradation percentage and adsorption capacity were calculated in percentage and mg g^{-1} bases, respectively.

$$\text{Degradation percentage}: R_p = \frac{C_0 - C_t}{C_0} \times 100 \quad (13)$$

$$\text{Degradation capacity}: q_e = \frac{C_0 - C_t}{W} \times V \quad (14)$$

3. Results and discussion

3.1. Characterization of pure and copper doped hydroxyapatite

Crystallographic analyses of the synthesized samples were performed using XRD, and the generated patterns (Fig. 1(A)) were confirmed by matching with those of the standard database (ICDD# 01-073-8419). All the synthesized HAp and Cu-doped HAp samples exhibited characteristic peaks at d-spacings of 3.44 (002), 2.81 (211), 2.77 (112), 2.72(300), 2.63 (202), 2.26 (130), 1.94 (222), and 1.84 (213), which match the standard pattern of HAp. The sharp peaks in the range from 30° to 34° represent a perfect crystal structure, and the doping of Cu into HAp reduced the intensity of the peaks in the XRD pattern in a gradual trend; the higher the Cu percentage, the lower the intensity. A similar XRD pattern also confirmed that the doping of copper into HAp did not change the phase and/or structure of the crystal. The lattice parameters, crystallinity, dislocation density, microstrain, crystallinity index, HAp percentage, β-TCP

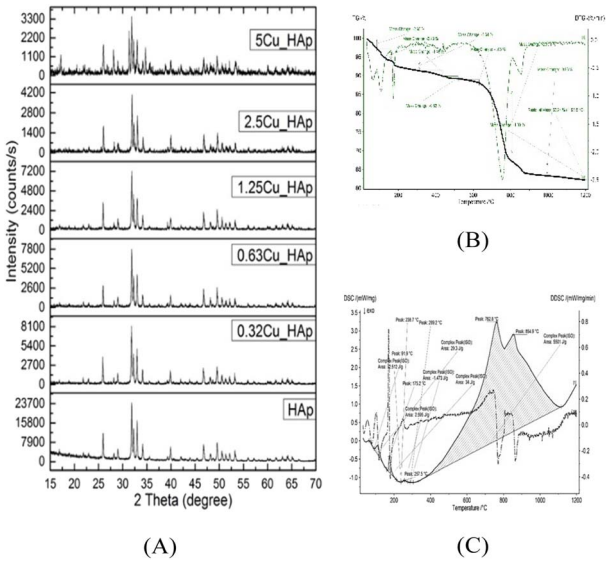

Fig. 1 (A) XRD patterns of pure and of Cu-doped HAp, and thermal analysis of uncalcined hydroxyapatite: (B) TG and DTG; (C) DSC and DDSC.

percentage, and volume fraction of β-TCP were estimated using eqn (4)–(11) and the computed values are documented in Table 1. In addition to Scherrer's equation, to calculate the crystallite size, various models such as the linear straight-line method of Scherrer's equation (SLMS), Monshi–Scherrer method (M–S), and William–Hall method (W–H) were employed, and the computed data are included in Table 1. Details of the model equations are explained with the respective figures (ESI Fig. S_1, S_2 and S_3) in the ESI text† under the heading "crystallite size calculation using various models". The larger crystallite size obtained with the linear straight-line method of Scherrer's equation made this model unacceptable but the rest of the models generated crystallite sizes in the acceptable range.

Fourier Transform Infrared (FTIR) spectra of the synthesized products were collected to ascertain the functional groups and they are included here in Fig. 2. The HAp sample contained only OH^- and PO_4^{3-} activating groups for generating spectra,[39] and similar spectra were also observed for the doped samples. Tetrahedral PO_4^{3-} ions have four fundamental modes of vibrations (ν_1 = symmetric stretching, ν_2 = symmetric bending, ν_3 = asymmetric stretching and ν_4 = asymmetric bending).[41] The peaks of PO_4^{3-} group were appeared as a well-defined doublet of ν_4 vibration at wavenumbers near 565 and 600 cm^{-1} as well as a shoulder at 630 cm^{-1} with small deviation from pure HAp when copper was dopped. This splitting of spectra indicated low site symmetry of the phosphate group representing more than one distinct site.[42] The most intense peak accompanied with two other peaks of HAp was witnessed in the fingerprint region of 960–1190 cm^{-1} representing phosphate ions,[42] and it was assigned as the normal mode of ν_1 and ν_3. All the synthesized samples revealed a strongest peak near 1022 cm^{-1} (ν_3) with two adjacent peaks at 960 cm^{-1} (ν_1) and 1090 cm^{-1} (ν_3). Another small peak was observed at 470 cm^{-1} for ν_2 vibration. Similar phosphate spectra and peaks were reported in the literature for HAp.[43] The hydroxyl group generated small peaks in the regions of 3000–3600 cm^{-1} and 1550–1700 cm^{-1}. Inelastic electronic transitions of PO_4^{3-} groups were also identified using Raman spectroscopy. Significant characteristic peaks of ν_1, ν_2, ν_3, and ν_4 modes were found in the Raman shifts of 963, 429, 1049, and 587 cm^{-1}, and those peak positions were very similar to the previously reported values.[44]

Raw uncalcined samples were subjected to thermal analysis where mass change and heat energy change were measured against temperature variation and the results are shown in Fig. 1(B) and (C). A total of 38% mass was lost in the range of 30–1200 °C and a distinct heat flow was also noticed within the range, revealing five endothermic peaks. At the first stage of temperature increase, weight loss (6%) and two endothermic peaks with small peak areas (visualized in DSC) were observed due to the extraction of free and bound water from the samples and this continued up to 150 °C. At 200 °C, all the physically and chemically bound water along with capillary and bulk water had evaporated, causing an overall mass loss of 8%. Another

Table 1 Crystallographic parameters of synthesized hydroxyapatite and copper doped hydroxyapatite

		Sample ID					
Parameter		HAp	0.32Cu_HAp	0.63Cu_HAp	1.25Cu_HAp	2.5Cu_HAp	5Cu_HAp
Crystallite size, D_c (nm)		63.06	64.58	43.81	49.98	45.65	61.19
Dislocation density (line per m^2)		0.25	0.23	0.54	0.40	0.47	0.26
Degree of crystallinity		6.14	6.60	3.82	3.06	2.33	5.61
Crystallinity index, CI_{XRD}		1.49	1.41	1.34	1.11	1.61	1.39
Percentage of HAp		85.59	83.64	90.49	86.56	87.35	88.71
Percentage of β-TCP		14.40	16.35	9.51	13.43	12.64	11.28
Volume fraction of β-TCP		1.69	1.70	1.67	1.68	1.68	1.66
Crystallite size using model (nm)	SLMS	1448	3620	1060	1448	2413	3620
	M–S	66.32	67.48	43.25	52.39	49.79	61.95
	W–H	67.71	62.18	45.70	48.14	53.43	54.07
Lattice parameters (Å)		$a = b = 9.43$, $c = 6.86$ $V = 530.94$	$a = b = 9.41$, $c = 6.87$ $V = 528.36$	$a = b = 9.41$, $c = 6.88$ $V = 527.77$	$a = b = 9.42$, $c = 6.86$ $V = 527.83$	$a = b = 9.38$, $c = 6.86$ $V = 523.56$	$a = b = 9.40$, $c = 6.86$ $V = 525.55$

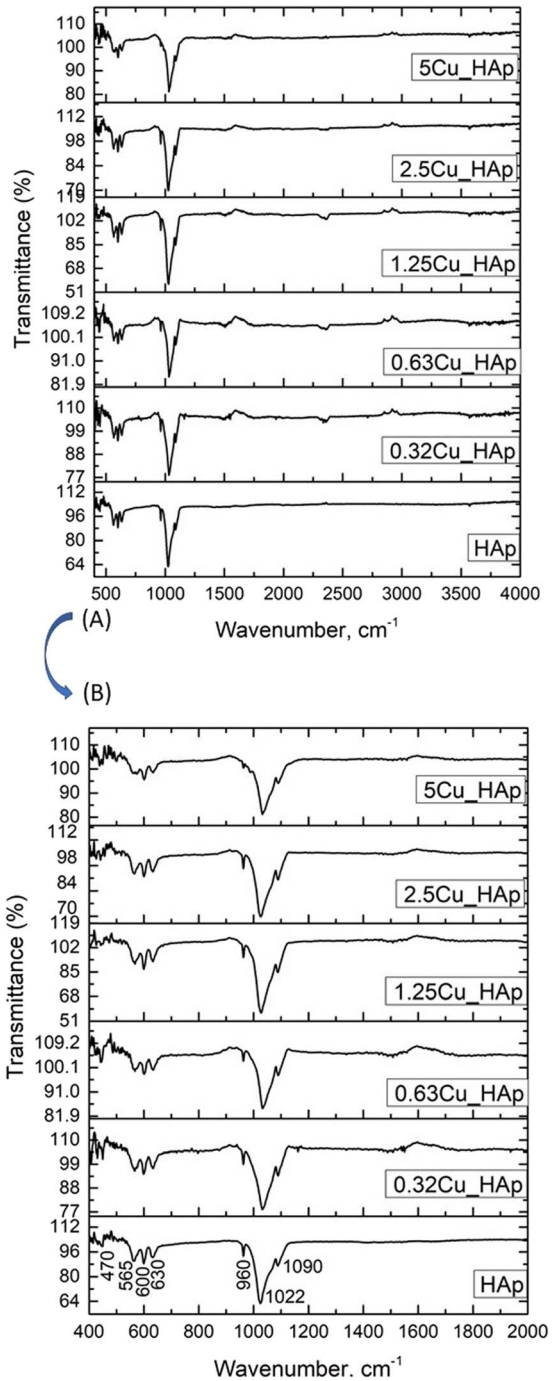

Fig. 2 FTIR spectra of pure and Cu-doped HAp: (A) full spectrum (400–4000 cm^{-1}) and (B) amplified spectrum (400–2000 cm^{-1}).

endothermic peak with a small peak area in DSC (apex 175 °C) was noticed in this region. No significant mass loss was detected up to 600 °C in the TGA plot, but a heat flow change was initiated at 400 °C and continued up to 1100 °C, displaying a huge peak area. Irreversible removal of lattice water owing to crystallization started after 600 °C and continued up to 900 °C with a mass loss of 25% along with two endothermic peaks. Similar thermal analyses were documented in the previously published literature.[45–47]

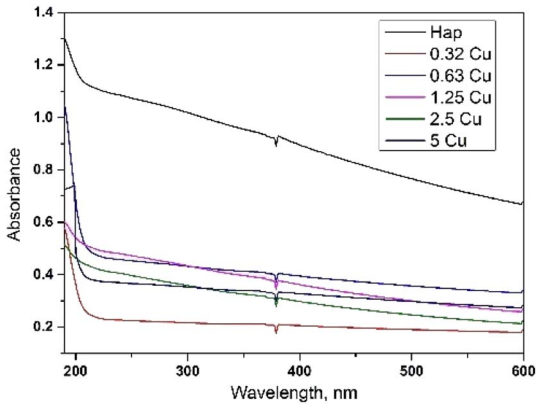

Fig. 3 UV-Vis spectra of the synthesized products.

The optical band gaps of the prepared products were estimated using eqn (14) and are included in the ESI files (Fig. S_4–S_9).† With the doping of copper into HAp, the band gap gradually decreased and thus the photocatalytic activity changed. The highest (5.77 eV) and the lowest (5.05 eV) band gaps were calculated for pure HAp and 5% Cu-HAp, respectively. The UV-Vis spectra are presented here in Fig. 3.

The surface morphology of the synthesized samples was investigated using SEM and is visualized in Fig. 4. All the captured pictures presented a small particle size, which was in tune with the crystallite size (45–65 nm) measured using the XRD technique. Only the particles of 0.32Cu_HAp were in a coalesced form, and the maximum particle size was also calculated using XRD. Homogeneity throughout the materials was observed as no foreign particles were found in the SEM images. All the samples exhibited rough surfaces maintaining sufficient vacant space, which defines a very crucial property of materials for applications such as sorption or photocatalysis. The nano-sized particles also stayed close due to quantum confinement, which significantly controls the characteristic of HAp[48] as well as the copper doped HAp. Variation in particle size and shape is a common factor for HAp and similar types of pictures were also reported in the literature.[49–51]

3.2. Photocatalytic activity of pure and copper doped hydroxyapatite

The photocatalytic activity of an adsorbent is prominently ruled by the adsorbent/solution ratio, which influences the capacity of an adsorbent in a batch operated system.[52] The degradation percentage and capacity were investigated by varying the photocatalyst dose from 0.1 to 0.5 g and using the experimental conditions as described for the adsorption study, and the relevant data are depicted in ESI Fig. S_12.† With the increment of catalyst dose, the degradation percentage increased linearly and the minimum (45%) and the maximum (93%) values were calculated for HAp and 0.63Cu_HAp, respectively. In contrast, the degradation capacity gradually subsided at a higher catalyst dose and the uppermost (8.4) and the lowermost (1.59) values were computed for 0.63Cu_HAp and HAp, respectively. When additional catalysts were present in the solution, the number of

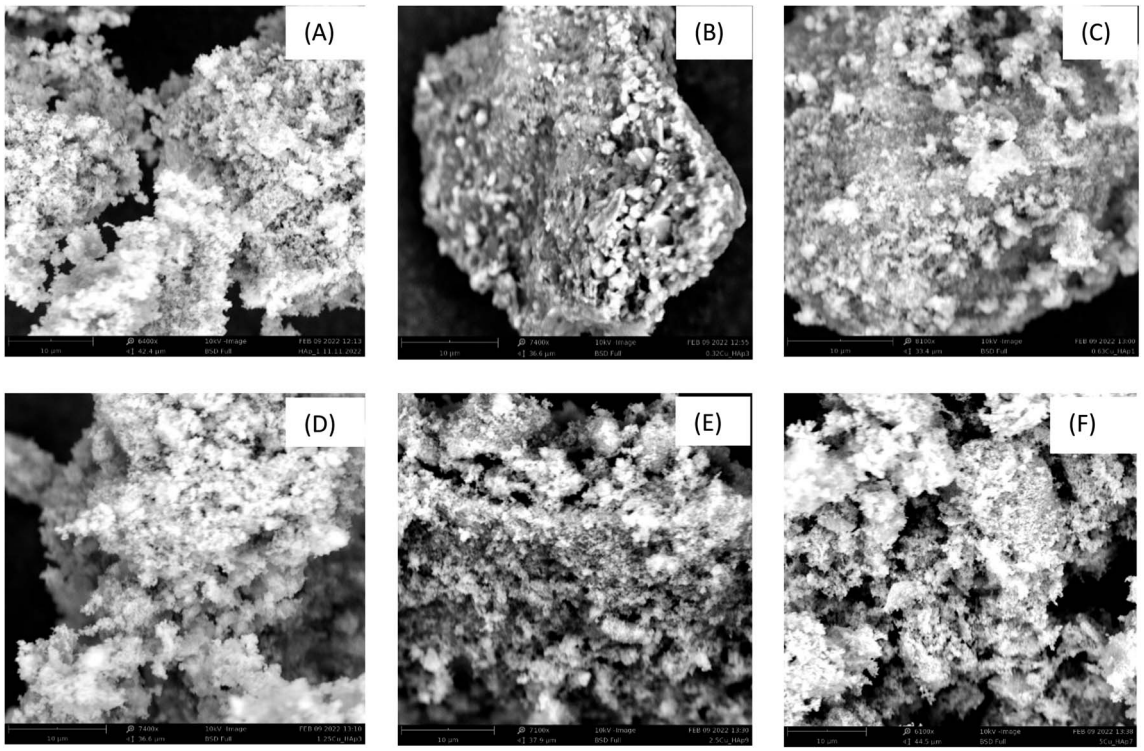

Fig. 4 Scanning electron microscopy images of (A) HAp, (B) 0.32Cu_HAp, (C) 0.63Cu_HAp, (D) 1.25Cu_HAp, (E) 2.5Cu_HAp, and (F) 5.0Cu_HAp with scale bars of 10 μm.

active sites escalated for adsorption resulting in augmented catalysis. The catalysis process is characterized by the adsorption and breakdown of Congo red dye (detailed explanations are documented later). On the other hand, with the augmentation of the initial concentration of Congo red dye, the degradation percentage dwindled but degradation capacity was amplified, and these phenomena are illustrated in ESI Fig. S_13.†

With increasing time, the photodegradation of Congo red dye increased linearly and was recorded up to 700 min starting from 30 min for two (0.1 and 0.2 g) photocatalyst doses. The highest degradation (99%) of the dye was calculated for the 0.63Cu_HAp sample at 700 min for 0.1 g of photocatalyst. In contrast, 99% degradation was computed for 0.2 g of 0.63Cu_HAp at 270 min of illumination exposure. After a few hours, the degradation reached its maximum limit. The photocatalyst dose greatly influenced the degradation, curtailing the time at a higher dose for maximum degradation. The higher dose (0.2 g) in photocatalysis exerted relatively higher photodegradation percentages with a lower degradation capacity, but opposite results were generated for the lower dose (0.1 g). Considering the timeframe and degradation percentages along with degradation capacity, the higher photocatalyst dose (0.2 g) and 180 min were carefully chosen for further investigation. The removal percentage of 0.1 and 0.2 g of photocatalyst is illustrated in ESI Fig. S_14 and S_15,† respectively, and the subsequent removal capacity is documented in ESI Fig. S_16 and S_17.†

Photochemical reactions under a light source in the presence of a photocatalyst are greatly influenced by the pH of the solution and the dependency of degradation percentage on pH is illustrated in ESI Fig. S_18† and that of degradation capacity is appended in ESI Fig. S_19.† When the pH value was very low (pH 3) or high (pH 9 and 11), the degradation percentage and capacity were low, and at medium pH (pH 5 and 7), the values were maximum for all the prepared samples. Thus, the excess hydrogen and hydroxyl ions played a significant role in the photochemical reaction induced by pure and Cu-HAp. pH 7 was chosen as the optimum value as the other values needed extra effort as well as additional cost of acidic solution.

Experiment under solar irradiation. The photocatalytic efficacy of pure and Cu-HAp was also estimated under solar irradiation and is visualized here in Fig. 5. Relatively higher degradation percentages and capacity were observed under sunlight than under the simulated sunlight. The maximum values of photodegradation (99%) and degradation capacity (4.9 mg g^{-1}) were calculated for 0.63Cu_HAp at 180 min irradiation time in 50 mL of 20 ppm dye solution. Though better degradation resulted from solar radiation, it is not industrially feasible for industrial wastewater purification to be performed under varying light during the day and night. The intensity of sunlight varies depending on different parameters, which can also be a hindrance for the estimation of photonic efficiency of synthesized products and thus a fixed light source was chosen.

Effects of temperature. Variations in temperature (15–60 °C) were also studied to observe the photocatalytic activity of pure and doped HAp and the results are illustrated in ESI Fig. S_20,† which shows a graph of degradation percentage and degradation capacity against temperature. No significant variation in degradation percentage or degradation capacity provided good

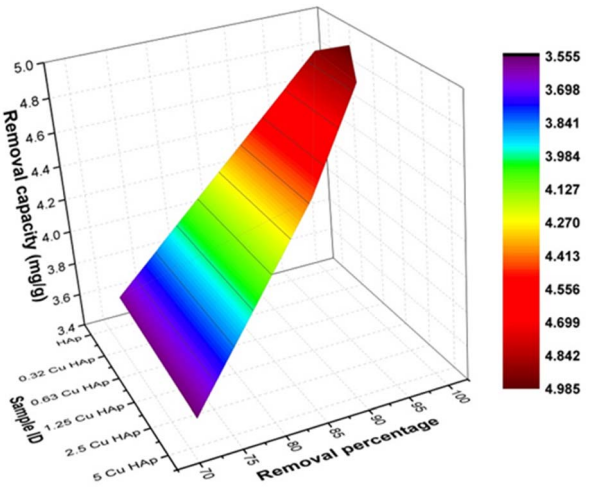

Fig. 5 Photocatalytic degradation percentage and photocatalytic capacity under solar irradiation.

evidence that the reaction temperature failed to greatly influence the photocatalytic performance of the prepared samples maintaining 0.2 g of photocatalyst, 180 min illumination time, and 50 mL of 20 ppm Congo red dye solution.

Reuse study. The reusability of the catalyst was studied following the same procedure as described for the estimation of the effects of time. In brief, the catalyst was filtered out from the aqueous solution and dried under normal sunlight for 6 h and after that the catalyst was used for another batch reaction. The recycling property of pure and 0.63Cu_HAp was explored using an average of at least 5 samples for each type and is visualized here in Fig. 6 and ESI Fig. S_21† in terms of degradation percentage and degradation capacity, respectively. The degradation percentage and capacity of the HAp samples dwindled from 65% to 40% and 3.2 mg g^{-1} to 1.99 mg g^{-1}, respectively. A gradual decrease of degradation percentage and capacity was also estimated for 0.63Cu_HAp from 91% to 67% and 4.6 mg g^{-1} to 3.4 mg g^{-1}, respectively. After three cycles of reuse, 0.63% copper doping can enable photocatalytic efficiency more than that of pure HAp.

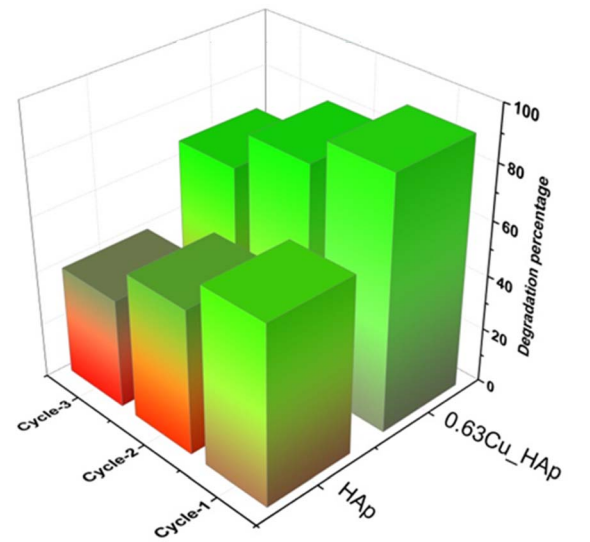

Fig. 6 Reuse property of pure HAp and 0.63Cu_HAp in terms of degradation percentage.

3.3. Molar absorption co-efficient of Congo red dye

The molar absorption coefficient (ε) defines the characteristic behavior of materials in terms of radiation energy absorption at a particular wavelength. The molar absorption coefficient of Congo red dye was calculated by employing the Beer–Lambert law[53] in the UV-Vis range, and the details are included in the ESI text† under the "Beer–Lambert law" heading. The molar absorptivity of Congo red dye was calculated at various pH (ESI Fig. S_22†) and at different initial dye concentrations (Fig. 7). The apex value of Congo red dye in UV absorption was witnessed at 498 nm and, consequently, the uppermost molar extinction coefficient (37 804 L mol^{-1} cm^{-1}) was calculated at this absorption band for pH 7. For pH 3 and pH 5, the molar extinction coefficients overlapped and a very low value was computed. Whether the medium is acidic or basic, the molar absorptivity was lower with respect to the neutral condition and this phenomenon may have resulted from the interaction of H^+/OH^- ions with the azo bonds of Congo red. A gradual change was noticed with variation of dye concentration, and the maximum value was estimated for the 20 ppm solution; in contrast, the minimal value was observed for the 100 ppm solution. A lower photocatalytic activity was recorded at very low and high pH values, which was discussed in the previous section. Following a similar trend, the molar extinction coefficient at higher and lower pH values was the minimum. There is no evidence of a relationship between molar absorptivity and photocatalysis as molar absorptivity is related to the light absorbing capacity and photocatalysts are well known for producing ions, radicals, electrons, holes, *etc.*, which affect the reaction.

The molar absorptivity changes when the wavelength changes, thus the average values were indispensable for better understanding and further applicability. The following equation (eqn (15)) was used to determine the average value.

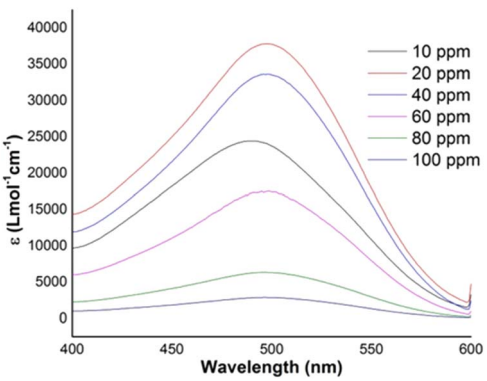

Fig. 7 Molar extinction coefficient of Congo red dye at a fixed pH of 7 and at various solution concentrations.

$$\varepsilon_{\text{average}} = \frac{\sum_{\lambda=400}^{\lambda_{\max}} \varepsilon\Delta\lambda}{\lambda_{\max} - 400} \quad (15)$$

Here, $\lambda_{\max}$ = maximum wavelength of absorption (in this case, 600 nm), and $\Delta\lambda$ = interval of wavelength during measurement. The average values of molar extinction coefficient are presented in the ESI file (Table S_1).†

3.4. Photodegradation kinetics

The photochemical degradation of organic pollutants in a watery medium has been explained in many pieces of literature focusing on the rate of reaction at distinct wavelengths. Richard G. Zepp *et al.* documented the rate of photochemical reaction[54] using eqn (16):

$$r = \left(-\frac{dC}{dt}\right) = E^0_{n,p,o}\left(\frac{S}{V}\right)\{1 - 10^{-[\alpha+\varepsilon C]l}\}\left\{\frac{\varepsilon C}{\alpha + \varepsilon C}\right\}\Phi \quad (16)$$

In eqn (16), r = rate of photochemical reaction, $\frac{dC}{dt}$ = rate of concentration change/rate of reaction, $E^0_{n,p,o}$ = photon fluence rate[55] (unit: moles per s per m^2 or einstein per s per m^2) = moles of photon (einstein) per unit time and per unit small cross-sectional area, S = surface area exposed to radiation (in m^2), V = volume of reactor (in L), α = absorption coefficient of solvent, ε = molar extinction coefficient of the photocatalyst, C = concentration of reactant, l = efficient path length of reaction medium, and Φ = quantum yield of direct photochemical reaction (dimensionless or mole einstein per s). The details of the equation are presented in the ESI file.†

Integration of the above equation results in eqn (17), which is the rate expression of a first order reaction.

$$\ln\frac{C}{C_0} = -K_1 t \quad (17)$$

where C_0 = initial concentration of reactant in mole per L, and C = final concentration of reactant in mole per L. The first-order rate constant (K_1) was estimated by plotting $-\ln\frac{C}{C_0}$ along the y-axis and time (t) along the x-axis and the generated graph is shown in Fig. 8 for 0.1 g of photocatalyst and in ESI Fig. S_23† for 0.2 g of photocatalyst. The computed rate constant and regression coefficient (R^2) are documented in Table 2 and the detailed values along with standard deviation are listed in ESI Tables S_2 and S_3† for 0.1 and 0.2 g of catalyst, respectively. The first order rate constant for 0.1 g of catalyst varied from 0.0015 to 0.0057 min^{-1} with a good correlation coefficient (minimum 0.945), while 0.2 g of photocatalyst had values from 0.0069 to 0.012 min^{-1} with a minimum regression coefficient of 0.95. The average values of the first-order rate constant were 0.00368 and 0.00697 min^{-1} for 0.1 and 0.2 g of photocatalyst, respectively, and the average values of rate constant increased by nearly double upon the addition of an extra 0.1 g of catalyst. This may be due to the generation of extra reacting species from the extra amount of photocatalyst. Abdallah Amedlous *et al.* reported more OH radical generation at higher temperatures[10] and this is in tune with our findings.

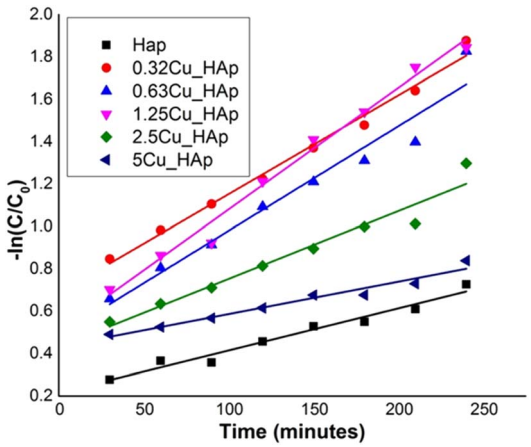

Fig. 8 Plot of $-\ln(C/C_0)$ against time (min) for various samples to calculate the reaction rate constant for 0.1 g of photocatalyst.

Table 2 First order rate constant (K_1) and regression coefficient (R^2) of the prepared samples at doses of 0.1 and 0.2 g of photocatalyst

	For 0.1 g of photocatalyst		For 0.2 g of photocatalyst	
Sample ID	K_1	R^2	K_1	R^2
HAp	0.00199	0.9631	0.00567	0.99286
0.32Cu_HAp	0.00467	0.98708	0.00265	0.99925
0.63Cu_HAp	0.00494	0.94516	0.00672	0.9985
1.25Cu_HAp	0.00474	0.98496	0.00752	0.95003
2.5Cu_HAp	0.00320	0.94525	0.01236	0.97622
5Cu_HAp	0.00153	0.95695	0.00689	0.98331
Average	0.00368	—	0.00696	—

The adsorption isotherm of Congo red under the previously mentioned conditions and at diverse initial concentrations was studied. Surface phenomena of a solid adsorbent and an adsorbate were assumed when employing various adsorption models such as the Freundlich adsorption isotherm[52] and Langmuir adsorption isotherm. The Freundlich adsorption isotherm can be expressed as follows (eqn (18)), and the details are documented in the ESI text:†

$$\log(q_e) = \log(K_F) + \frac{1}{n}\log(C_e) \quad (18)$$

The Freundlich adsorption isotherm is mainly applicable for heterogeneous surface sites and provides evidence for multi-layer adsorption.[52,56] By plotting $\log(q_e)$ against $\log(C_e)$ and establishing a straight line equation, the estimated values were obtained and are documented in Table 3, and the respective plot is shown in ESI Fig. S_24.† For homogeneous and single layer adsorption, the Langmuir adsorption isotherm is widely used. The linear form of the Langmuir adsorption isotherm can be expressed as eqn (19).[57]

$$\frac{C_e}{q_e} = \frac{1}{K_L\, q_{\max}} + \frac{C_e}{q_{\max}} \quad (19)$$

Table 3 Adsorption isotherm values and regression coefficient (R^2) of prepared samples utilizing different isotherm models

	Sample ID					
Isotherm model	HAp	0.32Cu_HAp	0.63Cu_HAp	1.25Cu_HAp	2.5Cu_HAp	5Cu_HAp
Freundlich isotherm	$K_F = 1.100$	$K_F = 2.169$	$K_F = 2.169$	$K_F = 1.781$	$K_F = 2.111$	$K_F = 1.347$
	$n = 1.375$	$n = 1.675$	$n = 1.67$	$n = 1.661$	$n = 1.579$	$n = 1.704$
	$R^2 = 0.92$	$R^2 = 0.91$	$R^2 = 0.91$	$R^2 = 95$	$R^2 = 0.89$	$R^2 = 0.91$
Langmuir isotherm	$K_L = 0.056$	$K_L = 0.094$	$K_L = 0.11$	$K_L = 0.070$	$K_L = 0.082$	$K_L = 0.069$
	$q_{max} = 14.9$	$q_{max} = 20.2$	$q_{max} = 24.3$	$q_{max} = 19.78$	$q_{max} = 23.0$	$q_{max} = 13.2$
	$R_L = 0.152$	$R_L = 0.096$	$R_L = 0.083$	$R_L = 0.124$	$R_L = 0.109$	$R_L = 0.127$
	$R^2 = 0.68$	$R^2 = 0.97$	$R^2 = 0.76$	$R^2 = 0.98$	$R^2 = 0.96$	$R^2 = 0.79$

Another dimensionless equilibrium parameter (R_L) can be calculated from the Langmuir adsorption constant (K_L) and mathematical expression of eqn (20).

$$R_L = \frac{1}{1 + K_L C_{max}} \quad (20)$$

The notation and details are included in the ESI text† under the heading Langmuir adsorption isotherm (ESI Fig. S_25†) and the calculated values are listed in Table 3.

3.5. Quantum yield or photonic efficiency

The value of the first-order rate constant, which was estimated in the previous section, is influenced by the experimental conditions,[58] thus a more fundamental parameter like quantum yield (Φ) is essential for a proper explanation of the photochemical reaction of any photocatalyst. Quantum yield describes the efficacy of a photochemical reaction and is defined as the number of moles of species that are transformed per number of moles of absorbed photons. Photonic efficacy or quantum yield is the interaction of photon energy with the photocatalyst and is defined by ignoring the scattering and reflecting radiation of the incident light source. Comparison of photonic efficacy among photocatalysts is possible if all the experimental runs are carried out in the same environment without varying the reactor or catalyst concentration.[59] In this research, photon energy was absorbed by the synthesized pure and Cu-HAp, which further generated reacting species that degraded the Congo red dye. Quantum yield was computed by employing eqn (21) and is shown here in Fig. 9. Photon fluence rate was similar for all the experimental data and thus quantum yield varied based on the reaction rate constant as well as molar extinction co-efficient.

$$\Phi = \frac{K_1}{2.303 E^0_{n,p,o}\left(\frac{S}{V}\right) l\varepsilon} \quad (21)$$

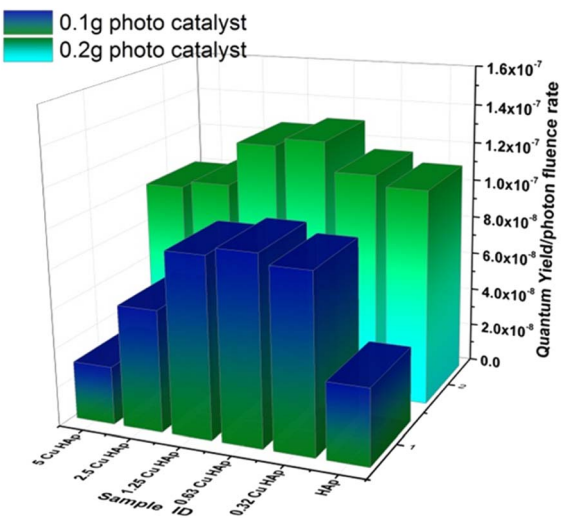

Fig. 9 Quantum yield/photon fluence rate of different types of samples.

In the mentioned graph, the quantum yield was calculated and is displayed only for the doses of 0.1 and 0.2 g of photocatalyst, and the plot provides good evidence that the photocatalyst dose contributed significantly to the photochemical reaction, which is in tune with the previously explained data. As the photon fluence rate was fixed, the higher number of moles of incident photon generated a greater number of moles of reacting species in the photocatalyst, which further resulted in increased dye degradation. Up to a certain limit of copper doping, the quantum yield gradually increased, and then it decreased, and this phenomenon can be explained in terms of crystallographic trends. The band gap of photocatalysts is another important influential factor for the quantum yield, and it can be modified by varying the required moles of photon (einstein) to overcome the forbidden band. The calculated minimum and maximum quantum yields under the fixed reaction conditions were 2.9×10^{-8} and 1.3×10^{-7} for 0.1 g of 5Cu_HAp and 0.2 g of 0.63Cu_HAp, respectively. The quantum yield of pharmaceutically active ingredients generally varies from 10^{-6} to 10^{-2} mole per einstein.[58,60] When a photon directly takes part in any degradation reaction, a higher quantum yield is observed, as is well explained in the literature. But, if an incident photon generates secondary reacting species, the quantum yield value will be lower, which was found in this research work.

To obtain more clarification of the result of quantum yield, another term, the space time yield (STY), was calculated from the ratio of quantum efficacy and photocatalyst mass.[61] The minimum and maximum values of STY were 2.9×10^{-7} and 6.5×10^{-7}, respectively.

4. Discussion

HAp, which is also known as calcium hydroxyapatite, is composed of hexagonal unit cells. When the copper doped products were synthesized, the only variation was the percentage of calcium due to the replacement of calcium by copper. The atomic radius of calcium (0.197 nm) was higher than that of copper (0.128 nm),[62,63] and this difference significantly changed the hexagonal crystal structure resulting in a dissimilarity in lattice parameters as well as other crystallographic parameters. The modifications in crystallographic parameters changed the photocatalytic activity of the products by varying the properties, for example the small crystallite size increased the surface area, the higher dislocation density created more crystal defects, the greater volume fraction of β-TCP curtailed the photocatalytic species in the sample, and the higher content of semiconductor materials in the crystals lowered the band gap energy. Thus, in this research, the photocatalytic efficacy of pure and Cu-HAp was meaningfully influenced by the mentioned properties. Generally, crystallite sizes are calculated using Scherrer's equation where only one plane is considered, and, in this study, the prime characteristic peak (211 plane) was taken into consideration, thus it cannot be representative of all crystal planes in a powder sample. To overcome this problem, a relationship was drawn with the degradation percentage of Congo red dye, dislocation density, and crystal size calculated from model equations where all the planes were taken into account. Both the Monshi–Scherrer method (M–S) and William–Hall method (W–H) model generated reasonable acceptable crystallite size values, and the relationship among degradation percentage, crystallite size and dislocation density is shown in ESI Fig. S_26 and S_27.† The picture presented higher degradation percentages when the crystallite sizes were small but the dislocation density was higher.

A correlation was also found between the percentages of pure and doped HAp, optical band gap energy, and degradation percentages of Congo red dye, and this is shown in ESI Fig. S_28.† With the copper doping, the optical band gap energy reduced gradually (documented in earlier text), so it was expected to have a higher photocatalytic activity due to the lower band gap. But, a lower percentage of HAp (higher percentage of β-TCP) limited the photocatalytic efficacy. Thus, the maximum efficiency of the products was observed when 0.63% copper was doped and thus the percentage content of HAp was maximum (90%) and optical band gap was 5.57 eV. The degree of crystallinity and crystallinity index also influenced the degradation percentage, thus when those values were lower, the degradation percentages were greater and the dependency is illustrated in ESI Fig. S_29.†

To obtain a better understanding of the degradation efficacy of the pure HAp and Cu-doped HAp, the ratio of the concentration of dye in aqueous medium and in solid medium was assessed, which is widely known as the partition coefficient.[64–66] The partition coefficients of the pure HAp and 0.63% Cu-doped HAp were 0.41 and 2.39, respectively.

In the photodegradation procedure, the advanced oxidation process acted as a sensitizer for redox reaction for the breakdown of Congo red dye under a photon source. The higher photon absorbing ability and lower recombining property of the photocatalyst effectively enhanced the photodegradation efficacy.[40] The previously calculated data of quantum yield or photonic efficacy of the prepared samples were an important driving force for the photocatalyst, where the maximum value was documented for 0.63% copper doped hydroxyapatite. Incident photons excited the surface electrons of the photocatalyst, which initiated the catalysis process. A simplified reaction mechanism was proposed for the degradation of Congo red utilizing pure and Cu-HAp and is shown in eqn (22)–(28).

$$Ca_{10}(PO_4)_6(OH)_2 \xrightarrow{\hbar\theta} Ca_{10}(PO_4)_6(OH_2) + e^- + h^+ \quad (22)$$

$$Ca_{x-y}Cu_y(PO_4)_6(OH)_2 \xrightarrow{\hbar\theta} Ca_{x-y}Cu_y(PO_4)_6(OH)_2 + e^- + h^+ \quad (23)$$

$$Ca_{10}(PO_4)_6(OH)_2/Ca_{x-y}Cu_y(PO_4)_6(OH)_2 + e^- + h^+ \rightarrow \cdot OH^{\bullet} + \cdot O_2 + \cdot OH^- \quad (24)$$

$$e^- + h^+ + H_2O \rightarrow \cdot O_2 + \cdot OH^- + \cdot O_2^- + H^+ + OH^- \quad (25)$$

$$\cdot OH^- + \cdot OH^- \rightarrow H_2O_2 \quad (26)$$

$$H_2O_2 + e^- + h^+ \rightarrow \cdot OH^{\bullet} + \cdot OH^- \quad (27)$$

$$\cdot OH^{\bullet} + \cdot O_2 + \cdot OH^- + \cdot O_2^- + e^- + h^+ + \text{Congo red dye} \rightarrow \text{intermediate} \rightarrow CO_2 + H_2O \quad (28)$$

The free radicals and electrons along with the holes can act as photocatalytic agents for the degradation of Congo red dye. The holes generated from the excitation of electrons from the valence band (VB) to the conduction band (CB) can act as strong oxidizing agents. The delay in recombination of e^- and h^+ generates more reacting species as the photon continues to be absorbed by the photocatalyst. This recombination of e^- and h^+ depends on the energy of the VB and CB, and mathematically can be expressed as eqn (29) and (30) according to Mulliken's theory:[67]

$$E_{CB} = X - E^e - 0.5E_{bg} \quad (29)$$

$$E_{VB} = E_{CB} + E_{bg} \quad (30)$$

where E_{VB}, E_{CB}, E^e, X, and E_{bg} are the energy of the valence band, conduction band, free electron energy (4.5 eV), the electronegativity of the photocatalyst, and band gap energy, respectively.

The electronegativity of pure and Cu-HAp was assumed to be the same as very low percentages of copper were added. The value (5.89 eV) was the geometric mean of its constituting element as described in the literature.[67] The calculated potentials of the valence band and the conduction band are listed in Table 4.

All the samples presented more negative potentials of CB than that of the redox potential of $O_2/\cdot O_2^-$ (−0.33 eV (ref. 22))

Table 4 Potential of valence band (VB) and conduction band (CB)

	Potential (eV)	
Sample ID	Valence band	Conduction band
HAp	4.275	−1.495
0.32Cu_HAp	4.185	−1.405
0.63Cu_HAp	4.175	−1.395
1.25Cu_HAp	4.005	−1.225
2.5Cu_HAp	3.955	−1.175
5Cu_HAp	3.91	−1.13

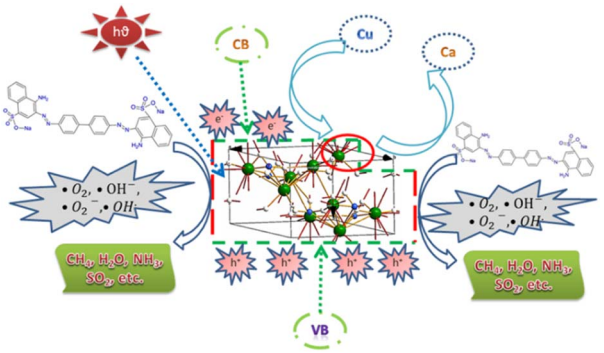

Fig. 10 Photocatalytic activity of pure and Cu-HAp.

and more positive potentials of the VB than that of OH/·OH (1.99 eV (ref. 22)) and thus both radicals can be formed for the photocatalysis of Congo red dye utilizing pure and Cu-HAp. A graphical representation of the catalytic activity of pure and Cu-HAp is illustrated in Fig. 10. This study was compared with other work, which is shown in Table 5.

A radical scavenger test was performed using isopropyl alcohol (IPA) in different volumes (5, 10, 15 mL) with the optimum parameters (50 mL of 20 ppm dye, 180 min, and 0.1 g of catalyst) for HAp and 0.63Cu_HAp. With the addition of IPA, the degradation percentage greatly decreased, and the higher the volume, the lower the degradation percentage. The effects of adding a radical scavenger on the performance of HAp and 0.63Cu_HAp are shown in Fig. 11. 65% and 91% degradation was observed for HAp and 0.63Cu_HAp, respectively, and with

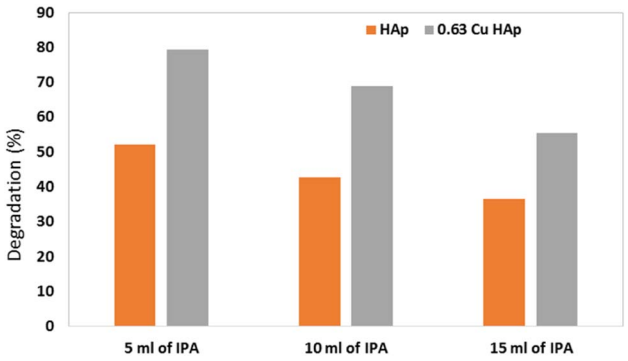

Fig. 11 Effects of IPA on photodegradation.

the addition of 5 mL of IPA, the degradation dwindled to 52% and 79% for the respective samples.

5. Practical implications of this study

This study was carried out on the laboratory scale and hence more data will be required for the treatment of real industrial wastewater where a mixture of a number of organic and inorganic compounds is present. Further, this study can be reproduced using different types of pollutant such as adipic acid, caprolactam, benzoic acid, toluene, phenol, different types of cationic and anionic dye, benzene, ciprofloxacin, amoxicillin, *etc.* Before application in industrial sector, a number of literatures must be studied and a pilot plant study must be executed.

6. Conclusion

Copper doping in hydroxyapatite can prominently develop the photocatalytic efficacy of bio-ceramics, as all the doped products exerted higher catalytic activity. A few variables such as pH of the solution, contact time, catalytic dose, and initial dye concentration significantly influenced the activity, but ultrasonication and operating temperature failed to induce notable variation in the photocatalysis. This research also suggested that the crystal structure as well as band gap energy can be influential factors when selecting a photocatalyst. Very low quantum yields provided good evidence for the slow degradation of Congo red dye by the pure and copper doped

Table 5 Comparative study of photocatalytic efficacy of textile dyes

Catalyst	Condition	Deg. (%)	Dye[a]	Ref.
0.63Cu_HAp	180 min, 20 ppm, 0.1 g	99	CR	This study
Cu(2)-HAp	60 min, 10 ppm, 5 g L^{-1}	89	MB	10
Cu-HAp=PCL	70 min, 1 ppm	94.3	MB	19
Co–Ni-HAp	10 ppm, 1 g L^{-1}	88–98	MB	17
TiO_2	210 min, 40 ppm, 1 g L^{-1}	~90	CR	68
Co_3O_4/TiO_2/GO	90 min, 10 ppm, 0.25 g L^{-1}	91	CR	69
CS/*n*-CdS	180 min, 20 ppm, 1.5 g L^{-1}	86	CR	70
ZnO-based	240 min, 1 g L^{-1}	83	CR	71

[a] CR = Congo red, MB = methylene blue.

hydroxyapatite. The synthesized products retained good catalytic ability up to three cycles of reuse. As the maximum (99%) degradation of Congo red dye was noticed for the 0.63% copper doping level in hydroxyapatite, this percentage is suggested for the degradation of textile dye instead of pure hydroxyapatite. The findings of this research can be applied to degrade emerging contaminants such as antibiotics from pharmaceutical wastewater.

Author contributions

Md. Sahadat Hossain conceived and designed the experiment, analysed the data, wrote the original manuscript and performed experiments along with characterization with Supanna Malek Tuntun. Supanna Malek Tuntun synthesized and characterized the pure and copper doped hydroxyapatite, carried out the photocatalytic experiments, and assisted in draft writing of the manuscript. Newaz Mohammed Bahadur and Samina Ahmed supervised the findings of this work. Samina Ahmed supervised the overall work and assisted with writing the manuscript.

Conflicts of interest

There are no conflicts to declare.

Acknowledgements

The authors are grateful to Bangladesh Council of Scientific and Industrial Research (BCSIR) authority for financial support through R&D project (ref. no. 39.02.0000.011.14.134.2021/900; date: 30.12.2021). The authors are also grateful to Ministry of Science and Technology for approving special allocation project (ref. no. 39.00.0000.009.14.019.21-EAS-464-1211; date: 15.12.2021). Supanna Malek Tuntun wishes to thank the Department of Applied Chemistry and Chemical Engineering, Noakhali Science and Technology University, Noakhali, Bangladesh for approving the M.S. thesis program.

References

1 P. Govindasamy, B. Kandasamy, P. Thangavelu, S. Barathi, M. Thandavarayan, M. Shkir and J. Lee, Biowaste derived hydroxyapatite embedded on two-dimensional g-C3N4 nanosheets for degradation of hazardous dye and pharmacological drug *via* Z-scheme charge transfer, *Sci. Rep.*, 2022, **12**, 1–16.

2 Y. Xin and T. Shirai, Noble-metal-free hydroxyapatite activated by facile mechanochemical treatment towards highly-efficient catalytic oxidation of volatile organic compound, *Sci. Rep.*, 2021, **11**, 1–13.

3 E. G. Rodrigues, T. C. Keller, S. Mitchell and J. Perez-Ramirez, Hydroxyapatite, an exceptional catalyst for the gas-phase deoxygenation of bio-oil by aldol condensation, *Green Chem.*, 2014, **16**, 4870–4874.

4 K. Chen, M. Cao, C. Ding and X. Zheng, A green approach for the synthesis of novel Ag_3PO_4/SnO_2/porcine bone and its exploitation as a catalyst in the photodegradation of lignosulfonate into alkyl acids, *RSC Adv.*, 2018, **8**, 26782–26792.

5 M. Chahkandi, M. Zargazi, A. Ahmadi, E. Koushki and A. Ghasedi, In situ synthesis of holey gC_3N_4 nanosheets decorated by hydroxyapatite nanospheres as efficient visible light photocatalyst, *RSC Adv.*, 2021, **11**, 31174–31188.

6 M. Zahouily, W. Bahlaouan, B. Bahlaouan, A. Rayadh and S. Sebti, Catalysis by hydroxyapatite alone and modified by sodium nitrate: a simple and efficient procedure for the construction of carbon-nitrogen bonds in heterogeneous catalysis, *Arkivoc*, 2005, **13**, 150–161.

7 S. Sebti, R. Tahir, R. Nazih, A. Saber and S. Boulaajaj, Hydroxyapatite as a new solid support for the Knoevenagel reaction in heterogeneous media without solvent, *Appl. Catal., A*, 2002, **228**, 155–159.

8 T. Mitsudome, A. Noujima, T. Mizugaki, K. Jitsukawa and K. Kaneda, Supported gold nanoparticle catalyst for the selective oxidation of silanes to silanols in water, *Chem. Commun.*, 2009, 5302–5304.

9 A. N. Amenaghawon, C. L. Anyalewechi, H. Darmokoesoemo and H. S. Kusuma, Hydroxyapatite-based adsorbents: Applications in sequestering heavy metals and dyes, *J. Environ. Manage.*, 2022, **302**, 113989, DOI: 10.1016/j.jenvman.2021.113989.

10 A. Amedlous, O. Amadine, Y. Essamlali, H. Maati, N. Semlal and M. Zahouily, Copper loaded hydroxyapatite nanoparticles as eco-friendly fenton-like catalyst to effectively remove organic dyes, *J. Environ. Chem. Eng.*, 2021, **9**, 105501.

11 M. Bin Mobarak, Md. S. Hossain, Z. Yeasmin, M. Mahmud, Md. M. Rahman, S. Sultana, S. M. Masum and S. Ahmed, Probing the photocatalytic competency of hydroxyapatite synthesized by solid state and wet chemical precipitation method, *J. Mol. Struct.*, 2022, **1252**, 132142, DOI: 10.1016/j.molstruc.2021.132142.

12 C. E. Bekkali, H. Bouyarmane, M. E. Karbane, S. Masse, A. Saoiabi, T. Coradin and A. Laghzizil, Zinc oxide-hydroxyapatite nanocomposite photocatalysts for the degradation of ciprofloxacin and ofloxacin antibiotics, *Colloids Surf., A*, 2018, **539**, 364–370, DOI: 10.1016/j.colsurfa.2017.12.051.

13 A. E. Shalan, M. Afifi, M. M. El-Desoky and M. K. Ahmed, Electrospun nanofibrous membranes of cellulose acetate containing hydroxyapatite co-doped with Ag/Fe: Morphological features, antibacterial activity and degradation of methylene blue in aqueous solution, *New J. Chem.*, 2021, **45**, 9212–9220.

14 F. Elmi, B. Yousefi, M. M. Elmi, H. Alinezhad and Z. Moulana, Thermal decomposition synthesis of Zn-HAP (extracted from fish scale) nanopowder and its photocatalytic and antibacterial activities under visible light, *Ceram. Int.*, 2021, **47**, 21862–21872.

15 A. Rkhaila and B. Sallek, Antibacterial and photocatalytic performance of Silver orthophosphate/Hydroxyapatite composite, *Mediterr. J. Chem.*, 2019, **8**, 320–327.

16 H. Bouyarmane, C. El Bekkali, J. Labrag, I. Es-Saidi, O. Bouhnik, H. Abdelmoumen, A. Laghzizil, J. M. Nunzi

and D. Robert, Photocatalytic degradation of emerging antibiotic pollutants in waters by TiO_2/Hydroxyapatite nanocomposite materials, *Surf. Interfaces*, 2021, **24**, 101155.

17 M. S. Mohseni-Salehi, E. Taheri-Nassaj and M. Hosseini-Zori, Effect of dopant (Co, Ni) concentration and hydroxyapatite compositing on photocatalytic activity of titania towards dye degradation, *J. Photochem. Photobiol., A*, 2018, **356**, 57–70.

18 J. Kalita, B. Das and S. S. Dhar, Synergistic effect of iron and copper in hydroxyapatite nanorods for Fenton-like oxidation of organic dye, *Colloids Surf., A*, 2022, **643**, 128750.

19 H. A. Alrafai, Z. A. Al-Ahmed, M. K. Ahmed, M. Afifi, K. R. Shoueir and A. Abu-Rayyan, The degradation of methylene blue dye using copper-doped hydroxyapatite encapsulated into polycaprolactone nanofibrous membranes, *New J. Chem.*, 2021, **45**, 16143–16154.

20 S. Park, J. Choi, S. Mondal, T. M. T. Vo, H. Lee, S. Y. Nam, C.-S. Kim and J. Oh, The impact of Cu (II) ions doping in nanostructured hydroxyapatite powder: A finite element modelling study for physico-mechanical and biological property evaluation, *Adv. Powder Technol.*, 2022, **33**, 103405.

21 K. Vikrant and K.-H. Kim, Nanomaterials for the adsorptive treatment of Hg (II) ions from water, *Chem. Eng. J.*, 2019, **358**, 264–282.

22 S. Vigneshwaran, P. Sirajudheen, C. P. Nabeena and S. Meenakshi, In situ fabrication of ternary TiO2 doped grafted chitosan/hydroxyapatite nanocomposite with improved catalytic performance for the removal of organic dyes: Experimental and systemic studies, *Colloids Surf., A*, 2021, **611**, 125789.

23 R. H. Lindberg, S. Namazkar, S. Lage, M. Östman, Z. Gojkovic, C. Funk, F. G. Gentili and M. Tysklind, Fate of active pharmaceutical ingredients in a northern high-rate algal pond fed with municipal wastewater, *Chemosphere*, 2021, **271**, 129763.

24 O. Golovko, S. Örn, M. Sörengård, K. Frieberg, W. Nassazzi, F. Y. Lai and L. Ahrens, Occurrence and removal of chemicals of emerging concern in wastewater treatment plants and their impact on receiving water systems, *Sci. Total Environ.*, 2021, **754**, 142122.

25 N. A. Qasem, R. H. Mohammed and D. U. Lawal, Removal of heavy metal ions from wastewater: A comprehensive and critical review, *npj Clean Water*, 2021, **4**, 1–15.

26 P. Y. Nguyen, G. Carvalho, M. A. Reis and A. Oehmen, A review of the biotransformations of priority pharmaceuticals in biological wastewater treatment processes, *Water Res.*, 2021, **188**, 116446.

27 S. A. Khan, S. B. Khan and A. M. Asiri, Layered double hydroxide of Cd-Al/C for the mineralization and de-coloration of dyes in solar and visible light exposure, *Sci. Rep.*, 2016, **6**, 1–15.

28 R. Al-Tohamy, S. S. Ali, F. Li, K. M. Okasha, Y. A.-G. Mahmoud, T. Elsamahy, H. Jiao, Y. Fu and J. Sun, A critical review on the treatment of dye-containing wastewater: Ecotoxicological and health concerns of textile dyes and possible remediation approaches for environmental safety, *Ecotoxicol. Environ. Saf.*, 2022, **231**, 113160.

29 Y.-H. Lin and B.-H. Ho, Kinetics and Performance of Biological Activated Carbon Reactor for Advanced Treatment of Textile Dye Wastewater, *Processes*, 2022, **10**, 129.

30 G. V. Koulini, A. R. Laiju, S. T. Ramesh, R. Gandhimathi and P. V. Nidheesh, Effective degradation of azo dye from textile wastewater by electro-peroxone process, *Chemosphere*, 2022, **289**, 133152, DOI: **10.1016/j.chemosphere.2021.133152**.

31 C. F. Iscen, Ü. D. Gül, A. A. Yavuz and S. İlhan, Decolorization of dye solution containing Remazol Black B by Aspergillus niger isolated from hypersaline environment, *Int. J. Environ. Sci. Technol.*, 2022, **19**, 12497–12504, DOI: **10.1007/s13762-022-03929-y**.

32 N. El Messaoudi, M. El Khomri, A. Dabagh, Z. G. Chegini, A. Dbik, S. Bentahar, A. Lacherai, M. Iqbal, A. Jada, F. Sher and É. C. Lima, Synthesis of a novel nanocomposite based on date stones/CuFe2O4 nanoparticles for eliminating cationic and anionic dyes from aqueous solution, *Int. J. Environ. Stud.*, 2021, 1–19, DOI: **10.1080/00207233.2021.1929469**.

33 L. M. Biju, V. Pooshana, P. S. Kumar, K. V. Gayathri, S. Ansar and S. Govindaraju, Treatment of textile wastewater containing mixed toxic azo dye and chromium (VI) BY haloalkaliphilic bacterial consortium, *Chemosphere*, 2022, **287**, 132280, DOI: **10.1016/j.chemosphere.2021.132280**.

34 B. Louhichi, F. Gaied, K. Mansouri and M. R. Jeday, Treatment of textile industry effluents by Electro-Coagulation and Electro-Fenton processes using solar energy: A comparative study, *Chem. Eng. J.*, 2022, **427**, 131735, DOI: **10.1016/j.cej.2021.131735**.

35 R. Tanveer, A. Yasar, A.-B. Tabinda, A. Ikhlaq, H. Nissar and A.-S. Nizami, Comparison of ozonation, Fenton, and photo-Fenton processes for the treatment of textile dye-bath effluents integrated with electrocoagulation, *J. Water Process. Eng.*, 2022, **46**, 102547, DOI: **10.1016/j.jwpe.2021.102547**.

36 S. Perveen, S. Noreen, S. Shahid, H. Mehboob, S. Aslam, H. Iqbal and M. Bilal, Carrier-Free Cross-linked Laccase Crystals for Biocatalytic Degradation of Textile Industrial Effluents, *Appl. Biochem. Biotechnol.*, 2022, 1–15.

37 S. Li, P. L. Show, H. H. Ngo and S.-H. Ho, Algae-mediated antibiotic wastewater treatment: A critical review, *Environ. Sci. Ecotechnology*, 2022, 100145, DOI: **10.1016/j.ese.2022.100145**.

38 J. García, M. J. García-Galán, J. W. Day, R. Boopathy, J. R. White, S. Wallace and R. G. Hunter, A review of emerging organic contaminants (EOCs), antibiotic resistant bacteria (ARB), and antibiotic resistance genes (ARGs) in the environment: Increasing removal with wetlands and reducing environmental impacts, *Bioresour. Technol.*, 2020, **307**, 123228, DOI: **10.1016/j.biortech.2020.123228**.

39 M. Hossain, M. Mahmud, M. B. Mobarak and S. Ahmed, Crystallographic analysis of biphasic hydroxyapatite

synthesized by different methods: an appraisal between new and existing models, *Chem. Pap.*, 2021, 1–13.

40 S. Moshtaghi, M. Hamadanian and M. Salavati-Niasari, A simple hydrothermal route for the preparation of novel Na–Y–W nano-oxides and their application in dye degradation, *RSC Adv.*, 2022, **12**, 4913–4923, DOI: **10.1039/D1RA07645K**.

41 N. Kourkoumelis and M. T. Tzaphlidou, Spectroscopic Assessment of Normal Cortical Bone: Differences in Relation to Bone Site and Sex, *Sci. World J.*, 2010, **10**, 402–412.

42 I. Rehman and W. Bonfield, Characterization of hydroxyapatite and carbonated apatite by photo acoustic FTIR spectroscopy, *J. Mater. Sci.: Mater. Med.*, 1997, **8**, 1–4.

43 M. Petra, J. Anastassopoulou, T. Theologis and T. Theophanides, Synchrotron micro-FT-IR spectroscopic evaluation of normal paediatric human bone, *J. Mol. Struct.*, 2005, **733**, 101–110.

44 S. Sultana, M. S. Hossain, M. Mahmud, M. B. Mobarak, M. H. Kabir, N. Sharmin and S. Ahmed, UV-assisted synthesis of hydroxyapatite from eggshells at ambient temperature: cytotoxicity, drug delivery and bioactivity, *RSC Adv.*, 2021, **11**, 3686–3694.

45 M. S. Hossain, M. Mahmud, S. Sultana, M. Bin Mobarak, M. S. Islam and S. Ahmed, *R. Soc. Open Sci.*, 2021, **8**, 210684.

46 A. S. Khan, A. N. Hussain, L. Sidra, Z. Sarfraz, H. Khalid, M. Khan, F. Manzoor, L. Shahzadi, M. Yar and I. U. Rehman, Fabrication and *in vivo* evaluation of hydroxyapatite/carbon nanotube electrospun fibers for biomedical/dental application, *Mater. Sci. Eng., C*, 2017, **80**, 387–396, DOI: **10.1016/j.msec.2017.05.109**.

47 V. Prakash, I. Venda, V. Thamizharasi and E. Sathya, Influence of DMSO-Sr on the synthesis of hydroxyapatite by hydrothermal coupled microemulsion method, *J. Inorg. Organomet. Polym. Mater.*, 2021, **31**, 1095–1101.

48 S. Balhuc, R. Campian, A. Labunet, M. Negucioiu, S. Buduru and A. Kui, Dental Applications of Systems Based on Hydroxyapatite Nanoparticles—An Evidence-Based Update, *Crystals*, 2021, **11**, 674, DOI: **10.3390/cryst11060674**.

49 N. Y. Mostafa, Characterization, thermal stability and sintering of hydroxyapatite powders prepared by different routes, *Mater. Chem. Phys.*, 2005, **94**, 333–341, DOI: **10.1016/j.matchemphys.2005.05.011**.

50 N. Zheng, L. Yin, M. Su, Z. Liu, D. C. W. Tsang and D. Chen, Synthesis of shape and structure-dependent hydroxyapatite nanostructures as a superior adsorbent for removal of U(VI), *Chem. Eng. J.*, 2020, **384**, 123262, DOI: **10.1016/j.cej.2019.123262**.

51 J. Ali, H. Wang, J. Ifthikar, A. Khan, T. Wang, K. Zhan, A. Shahzad, Z. Chen and Z. Chen, Efficient, stable and selective adsorption of heavy metals by thio-functionalized layered double hydroxide in diverse types of water, *Chem. Eng. J.*, 2018, **332**, 387–397.

52 M. A. Darweesh, M. Y. Elgendy, M. I. Ayad, A. M. M. Ahmed, N. K. Elsayed and W. A. Hammad, Adsorption isotherm, kinetic, and optimization studies for copper (II) removal from aqueous solutions by banana leaves and derived activated carbon, *S. Afr. J. Chem. Eng.*, 2022, **40**, 10–20, DOI: **10.1016/j.sajce.2022.01.002**.

53 R. Delgado, Misuse of Beer–Lambert Law and other calibration curves, *R. Soc. Open Sci.*, 2022, **9**, 211103, DOI: **10.1098/rsos.211103**.

54 R. G. Zepp, Quantum yields for reaction of pollutants in dilute aqueous solution, *Environ. Sci. Technol.*, 1978, **12**, 327–329.

55 J. R. Bolton and M. I. Stefan, Fundamental photochemical approach to the concepts of fluence (UV dose) and electrical energy efficiency in photochemical degradation reactions, *Res. Chem. Intermed.*, 2002, **28**, 857–870.

56 M. S. Rahaman, S. M. M. Hasnine, T. Ahmed, S. Sultana, M. A. Q. Bhuiyan, M. S. Manir, N. Ullah, S. K. Sen, M. N. Hossain and M. S. Hossain, Radiation crosslinked polyvinyl alcohol/polyvinyl pyrrolidone/acrylic acid hydrogels: swelling, crosslinking and dye adsorption study, *Iran. Polym. J.*, 2021, 1–16.

57 A. Arabpour, S. Dan and H. Hashemipour, Preparation and optimization of novel graphene oxide and adsorption isotherm study of methylene blue, *Arabian J. Chem.*, 2021, **14**, 103003, DOI: **10.1016/j.arabjc.2021.103003**.

58 A. C. Reina, A. B. Martínez-Piernas, Y. Bertakis, C. Brebou, N. P. Xekoukoulotakis, A. Agüera and J. A. S. Pérez, Photochemical degradation of the carbapenem antibiotics imipenem and meropenem in aqueous solutions under solar radiation, *Water Res.*, 2018, **128**, 61–70.

59 A. Cabrera-Reina, A. B. Martínez-Piernas, Y. Bertakis, N. P. Xekoukoulotakis, A. Agüera and J. A. S. Pérez, TiO2 photocatalysis under natural solar radiation for the degradation of the carbapenem antibiotics imipenem and meropenem in aqueous solutions at pilot plant scale, *Water Res.*, 2019, **166**, 115037.

60 X.-H. Wang and A. Y.-C. Lin, Phototransformation of cephalosporin antibiotics in an aqueous environment results in higher toxicity, *Environ. Sci. Technol.*, 2012, **46**, 12417–12426.

61 V. Kumar, V. Singh, K.-H. Kim, E. E. Kwon and S. A. Younis, Metal-organic frameworks for photocatalytic detoxification of chromium and uranium in water, *Coord. Chem. Rev.*, 2021, **447**, 214148.

62 nglos324 – copper, (n.d.), **https://www.princeton.edu/~maelabs/mae324/glos324/copper.htm**, accessed March 12, 2022.

63 nglos324 – calcium, (n.d.), **https://www.princeton.edu/~maelabs/mae324/glos324/calcium.htm**, accessed March 12, 2022.

64 M. Al-Wabel, J. Elfaki, A. Usman, Q. Hussain and Y. S. Ok, Performance of dry water-and porous carbon-based sorbents for carbon dioxide capture, *Environ. Res.*, 2019, **174**, 69–79.

65 D. J. O'Connor and J. P. Connolly, The effect of concentration of adsorbing solids on the partition coefficient, *Water Res.*, 1980, **14**, 1517–1523.

66 S. A. Younis, E. A. Motawea, Y. M. Moustafa, J. Lee and K.-H. Kim, A strategy for the efficient removal of chlorophenols in petrochemical wastewater by

organophilic and aminated silica@ alginate microbeads: Taguchi optimization and isotherm modeling based on partition coefficient, *J. Hazard. Mater.*, 2020, **397**, 122792.

67 J. Soares da Silva, T. R. Machado, T. A. Martins, M. Assis, C. C. Foggi, N. G. Macedo, H. Beltran-Mir, E. Cordoncillo, J. Andres and E. Longo, α-$AgVO_3$ decorated by hydroxyapatite $(Ca_{10}(PO_4)_6(OH)_2)$: tuning its photoluminescence emissions and bactericidal activity, *Inorg. Chem.*, 2019, **58**, 5900–5913.

68 H. Guo, K. Lin, Z. Zheng, F. Xiao and S. Li, Sulfanilic acid-modified P_{25} TiO_2 nanoparticles with improved photocatalytic degradation on Congo red under visible light, *Dyes Pigm.*, 2012, **92**, 1278–1284.

69 W.-K. Jo, S. Kumar, M. A. Isaacs, A. F. Lee and S. Karthikeyan, Cobalt promoted TiO_2/GO for the photocatalytic degradation of oxytetracycline and Congo Red, *Appl. Catal., B*, 2017, **201**, 159–168.

70 H. Zhu, R. Jiang, L. Xiao, Y. Chang, Y. Guan, X. Li and G. Zeng, Photocatalytic decolorization and degradation of Congo Red on innovative crosslinked chitosan/nano-CdS composite catalyst under visible light irradiation, *J. Hazard. Mater.*, 2009, **169**, 933–940.

71 N. F. Khairol, N. Sapawe and M. Danish, Photocatalytic study of ZnO-CuO/ES on degradation of Congo red, *Mater. Today: Proc.*, 2019, **19**, 1333–1339.